SFN_list_20241011-20241014：工藤哲洋

38. arXiv:2410.08881 [pdf, other] astro-ph.EP astro-ph.SR doi 10.1093/mnras/stae2325

Atmospheric escape in hot Jupiters under sub-Alfvénic interactions

Authors: Andrés Presa, Florian A. Driessen, Aline A. Vidotto

Abstract: Hot Jupiters might reside inside the Alfvén surface of their host star wind, where the stellar wind is dominated by magnetic energy. The implications of such a sub-Alfvénic environment for atmospheric escape are not fully understood. Here, we employ 3-D radiation-magnetohydrodynamic simulations and Lyman-α transit calculations to investigate atmospheric escape properties of magnetised hot Jupite… ▽ More

Submitted 11 October, 2024; **originally announced** October 2024.

Comments: 16 pages, 11 figures (including 2 in the appendix), 2 tables, accepted for publication in MNRAS

37. arXiv:2410.08943 [pdf, other] astro-ph.SR astro-ph.EP astro-ph.GA

BD+44 493: Chemo-Dynamical Analysis and Constraints on Companion Planetary Masses from WIYN/NEID Spectroscopy

Authors: Vinicius M. Placco, Arvind F. Gupta, Felipe Almeida-Fernandes, Sarah E. Logsdon, Jayadev Rajagopal, Erika M. Holmbeck, Ian U. Roederer, John Della Costa, Pipa Fernandez, Eli Golub, Jesus Higuera, Yatrik Patel, Susan Ridgway, Heidi Schweiker

Abstract: In this work, we present high-resolution (R~100,000), high signal-to-noise (S/N~800) spectroscopic observations for the well-known, bright, extremely metal-poor, carbon-enhanced star BD+44 493. We determined chemical abundances and upper limits for 17 elements from WIYN/NEID data, complemented with 11 abundances re-determined from Subaru and Hubble data, using the new, more accurate, stellar atmos… ▽ More

Submitted 11 October, 2024; **originally announced** October 2024.

Comments: 25 pages, 11 figures, accepted for publication on ApJ

Astrophysics > Earth and Planetary Astrophysics

[Submitted on 11 Oct 2024]

Atmospheric escape in hot Jupiters under sub-Alfvénic interactions

Andrés Presa, Florian A. Driessen, Aline A. Vidotto

Hot Jupiters might reside inside the Alfvén surface of their host star wind, where the stellar wind is dominated by magnetic energy. The implications of such a sub-Alfvénic environment for atmospheric escape are not fully understood. Here, we employ 3-D radiation-magnetohydrodynamic simulations and Lyman-α transit calculations to investigate atmospheric escape properties of magnetised hot Jupiters. By varying the planetary magnetic field strength (B_p) and obliquity, we find that the structure of the outflowing atmosphere transitions from a magnetically unconfined regime, where a tail of material streams from the nightside of the planet, to a magnetically confined regime, where material escapes through the polar regions. Notably, we find an increase in the planet escape rate with B_p in both regimes, with a local decrease when the planet transitions from the unconfined to the confined regime. Contrary to super-Alfvénic interactions, which predicted two polar outflows from the planet, our sub-Alfvénic models show only one significant polar outflow. In the opposing pole, the planetary field lines connect to the star. Finally, our synthetic Ly-α transits show that both the red-wing and blue-wing absorptions increase with B_p. Furthermore, there is a degeneracy between B_p and the stellar wind mass-loss rate when considering absorption of individual Lyman-α wings. This degeneracy can be broken by considering the ratio between the blue-wing and the red-wing absorptions, as stronger stellar winds result in higher blue-to-red absorption ratios. We show that, by using the absorption ratios, Lyman-α transits can probe stellar wind properties and exoplanetary magnetic fields.

- ホットジュピターから大気が惑星間空間へ放出される過程において，恒星風や惑星磁場がどのような影響を与えるかを調べた。特に，恒星風がSub-Alfvenic 速度の場合を調べた。

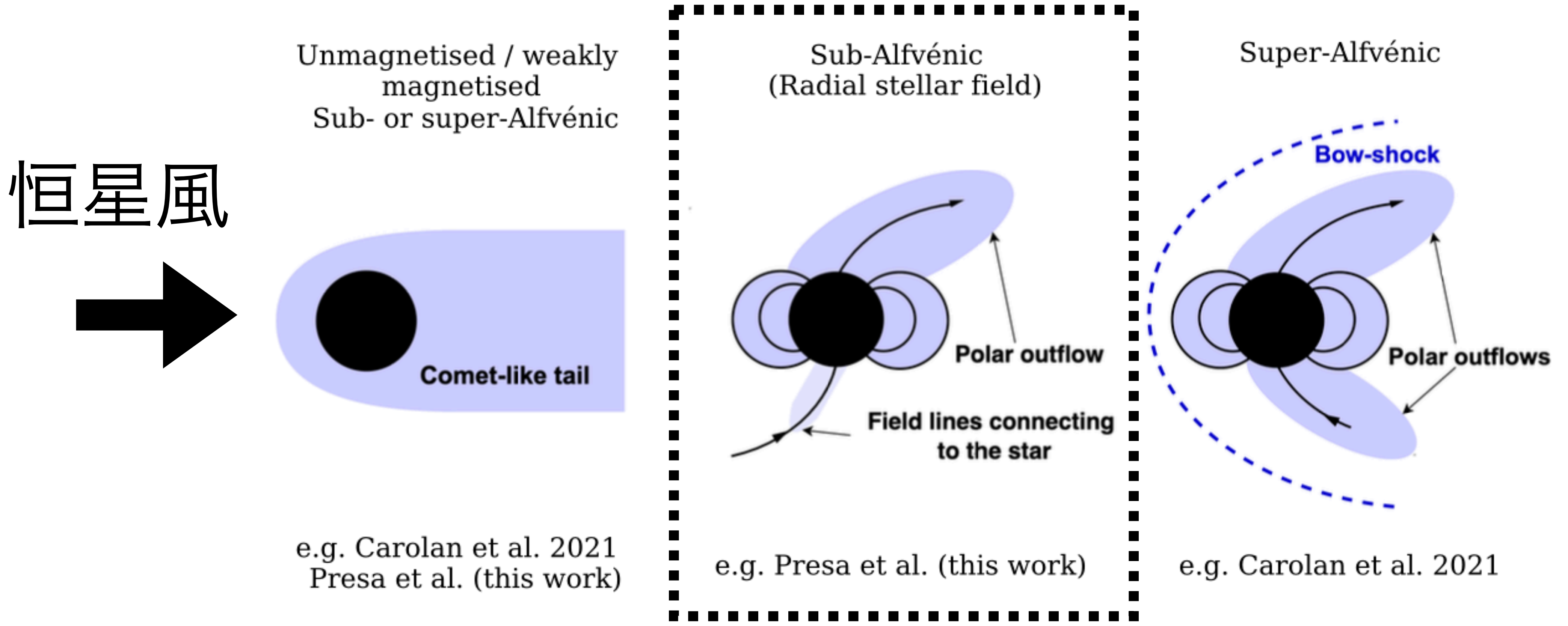

- Sub-Alfvenic な場合は，片方の極から大気の放出が起こりやすかった。

- 磁場が強いほうが，大気の放出率が大きくなった。磁極の公転軌道面に対する角度も，放出率に影響を与えた。

- 観測量としてLy-αの吸収を計算し，星風や系外惑星の性質を探る可能性を調べた。

基礎方程式

3D-MHD

$$\frac{\partial \rho}{\partial t} + \nabla \cdot \rho \mathbf{u} = 0,$$

$$\frac{\partial (\rho \mathbf{u})}{\partial t} + \nabla \cdot \left[\rho \mathbf{u}\mathbf{u} + \left(P + \frac{B^2}{8\pi} \right) I - \frac{\mathbf{B}\mathbf{B}}{4\pi} \right] = \rho \left(\mathbf{g} - \frac{GM_*}{|\mathbf{R}|^2} \hat{R} - \mathbf{\Omega} \times (\mathbf{\Omega} \times \mathbf{R}) - 2(\mathbf{\Omega} \times \mathbf{u}) \right),$$

$$\frac{\partial e}{\partial t} + \nabla \cdot \left[\mathbf{u} \left(e + P + \frac{B^2}{8\pi} \right) - \frac{(\mathbf{u} \cdot \mathbf{B})\mathbf{B}}{4\pi} \right] = \rho \left(\mathbf{g} - \frac{GM_*}{|\mathbf{R}|^2} \hat{R} - \mathbf{\Omega} \times (\mathbf{\Omega} \times \mathbf{R}) \right) \cdot \mathbf{u} + \mathcal{H} - \mathcal{C},$$

$$\frac{\partial \mathbf{B}}{\partial t} + \nabla \cdot (\mathbf{u}\mathbf{B} - \mathbf{B}\mathbf{u}) = 0,$$

加熱：恒星からのXUV

冷却：Ly-α，自由電子の衝突

$$\frac{\partial n_n}{\partial t} + \nabla \cdot n_n \mathbf{u} = \mathscr{R} - \mathscr{I},$$

イオン化

再結合

$$\frac{\partial n_p}{\partial t} + \nabla \cdot n_p \mathbf{u} = \mathscr{I} - \mathscr{R},$$

あとでLy-αの計算に必要

Table 1. The stellar and planetary parameters used in our models. M_p and R_p are the mass and radius of the planet; B_p is the polar dipole field strengths and obliquity describes the magnetic field obliquities; a is the orbital distance from the star, and $F_{\rm xuv}$ is the X-ray flux received by the planet. The stellar mass and radius are denoted by M_* and R_*, respectively. $\dot{M}_*$ and T_* describe the stellar wind mass-loss rate and temperature, and B_* is the stellar surface field strength (radial).

M_p (M_J)	R_p (R_J)	B_p (G)	Obliquity (°)	a (au)	$F_{\rm xuv}$ (erg/cm^2/s)	M_* ($M_\odot$)	R_* ($R_\odot$)	$\dot{M}_*$ ($M_\odot$/yr)	T_* (10^6 K)	B_* (G)
0.7	1.4	0.25–25	0, 45, 90, 135, 180	0.05	500	1.148	1.19	0, 2×10^{-13}	1	2

惑星大気： 根本固定1000K，2.4 x 10^{11} cm^{-3} の1次元モデル

初期に球対称でアウトフロー

惑星磁場： 初期に双極子磁場

恒星風： 太陽と似た thermal wind，境界から流入

（恒星風がある場合とない場合で比較している）

恒星風なし（左から恒星の光に照らされている）

色は密度，矢印は磁力線

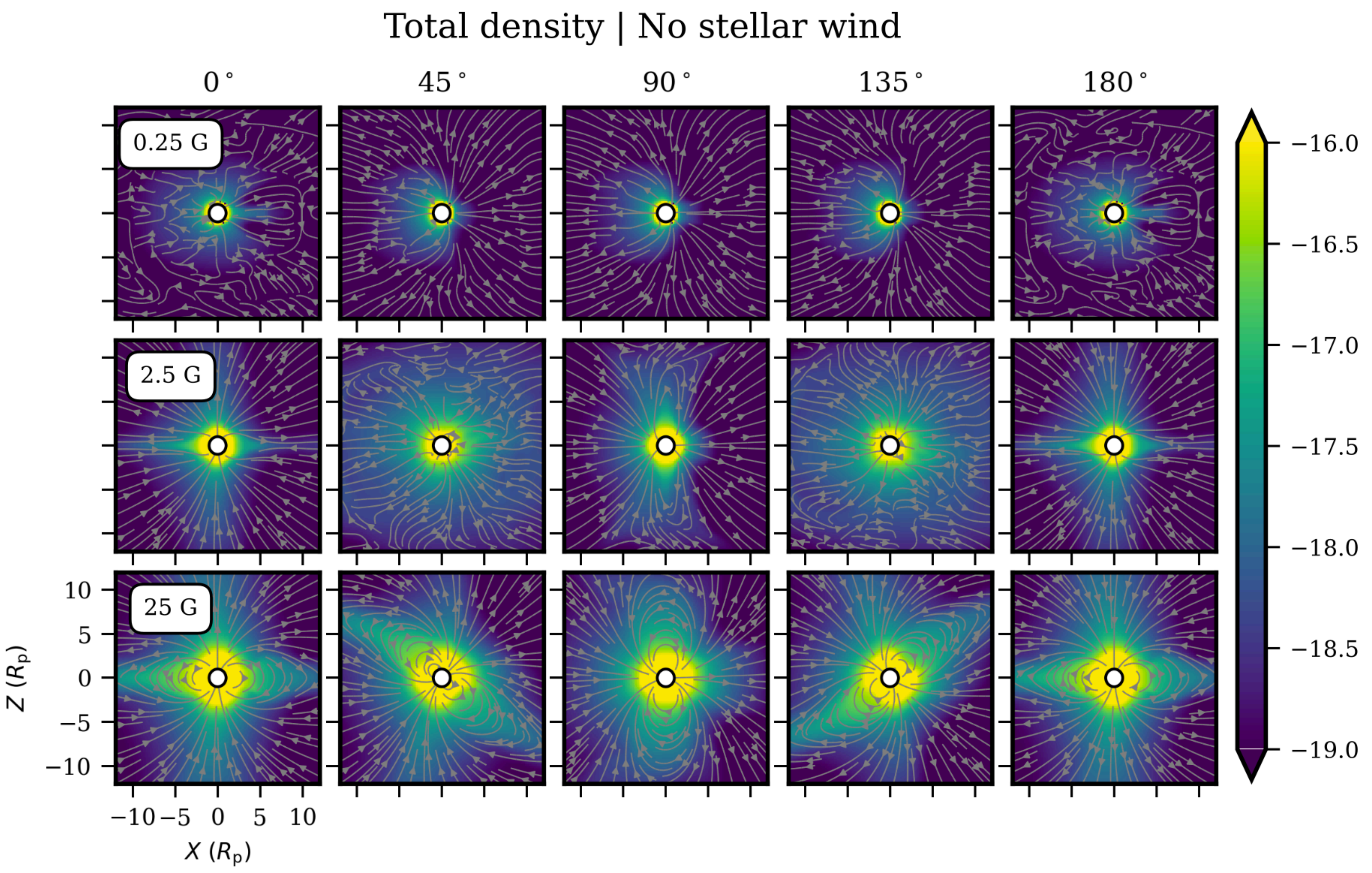

色は加熱率，矢印は流線

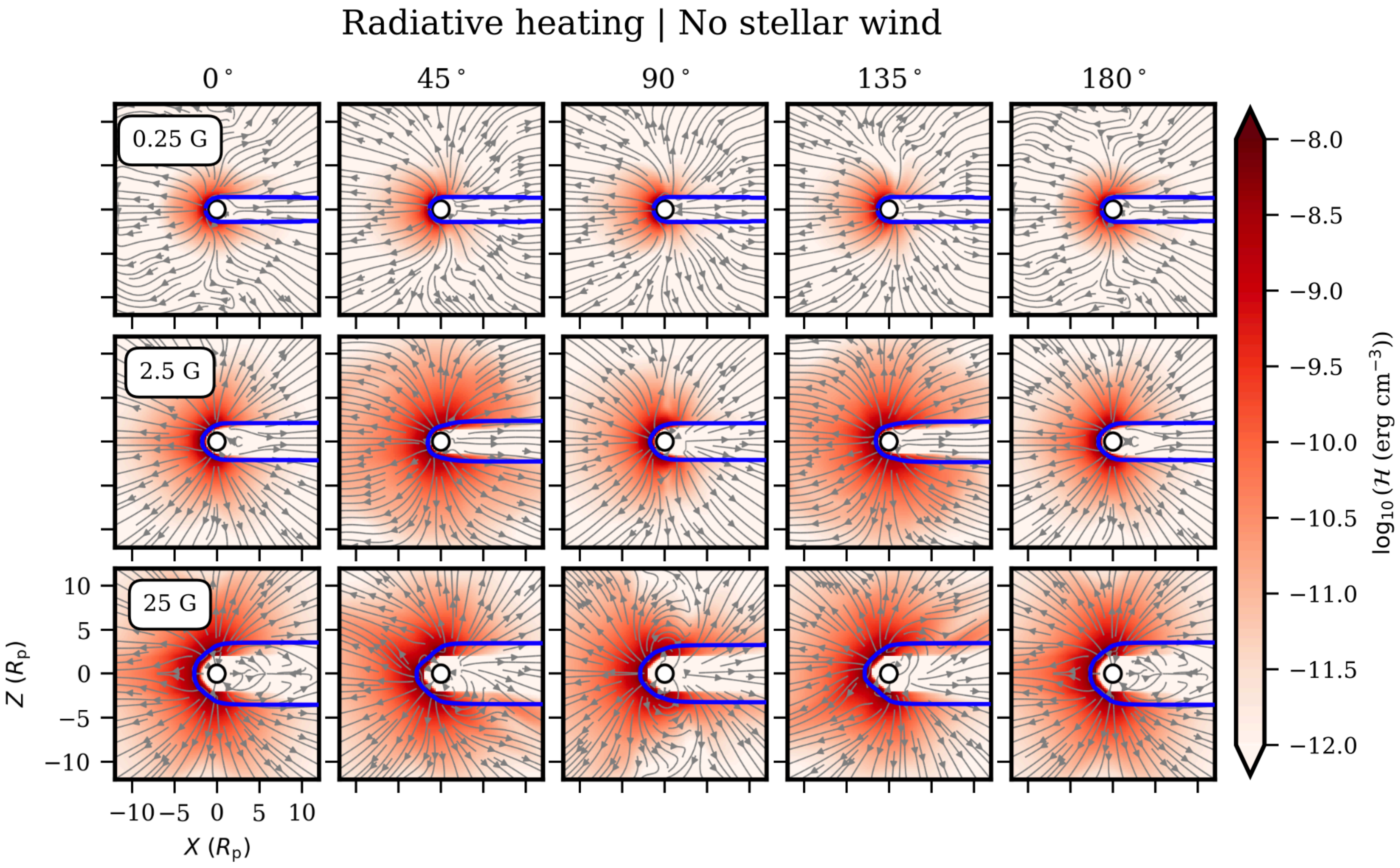

青線は，Ly-αのτ=1

恒星風あり（左から恒星風と恒星光）

色は密度，矢印は磁力線

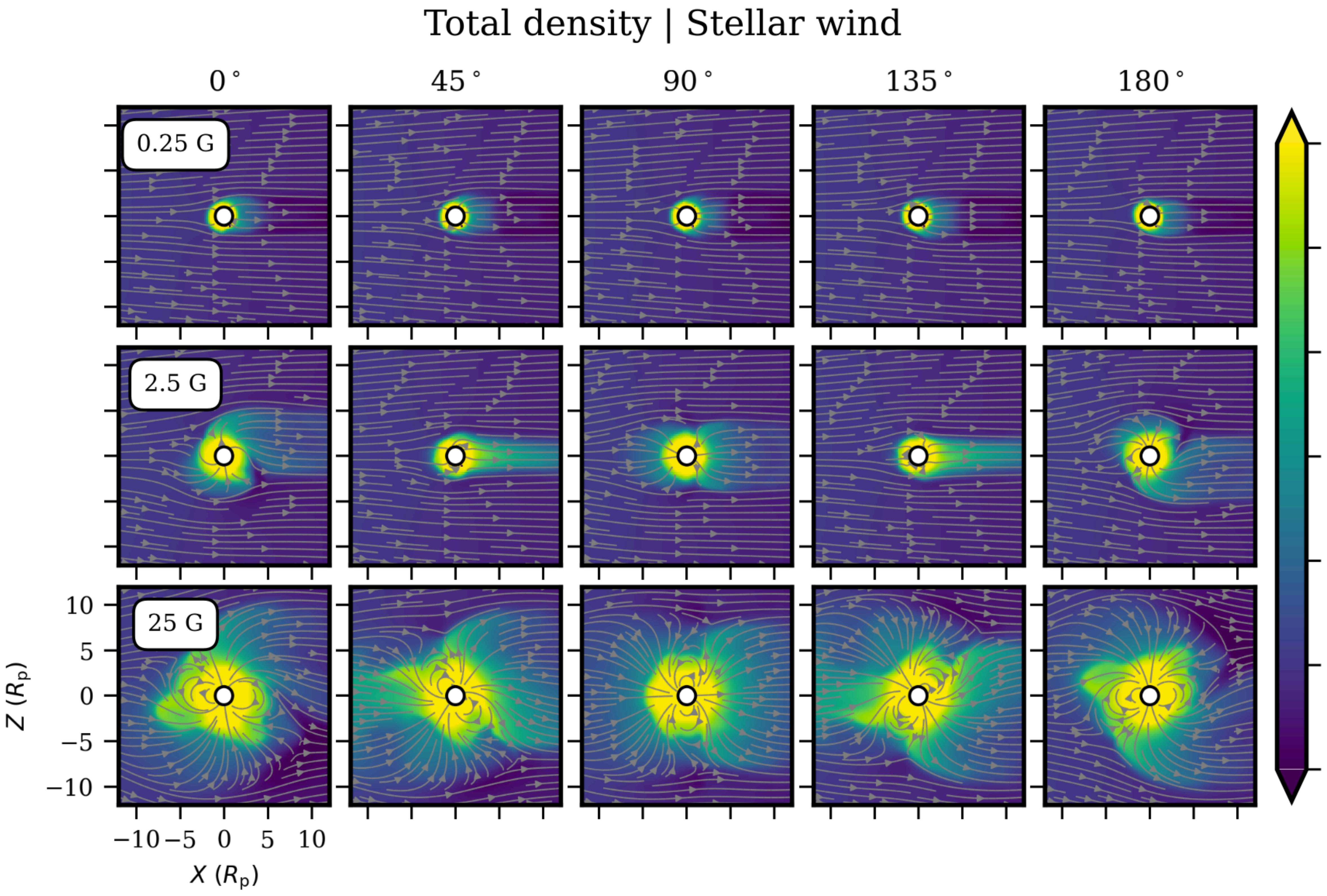

色は加熱率，矢印は流線

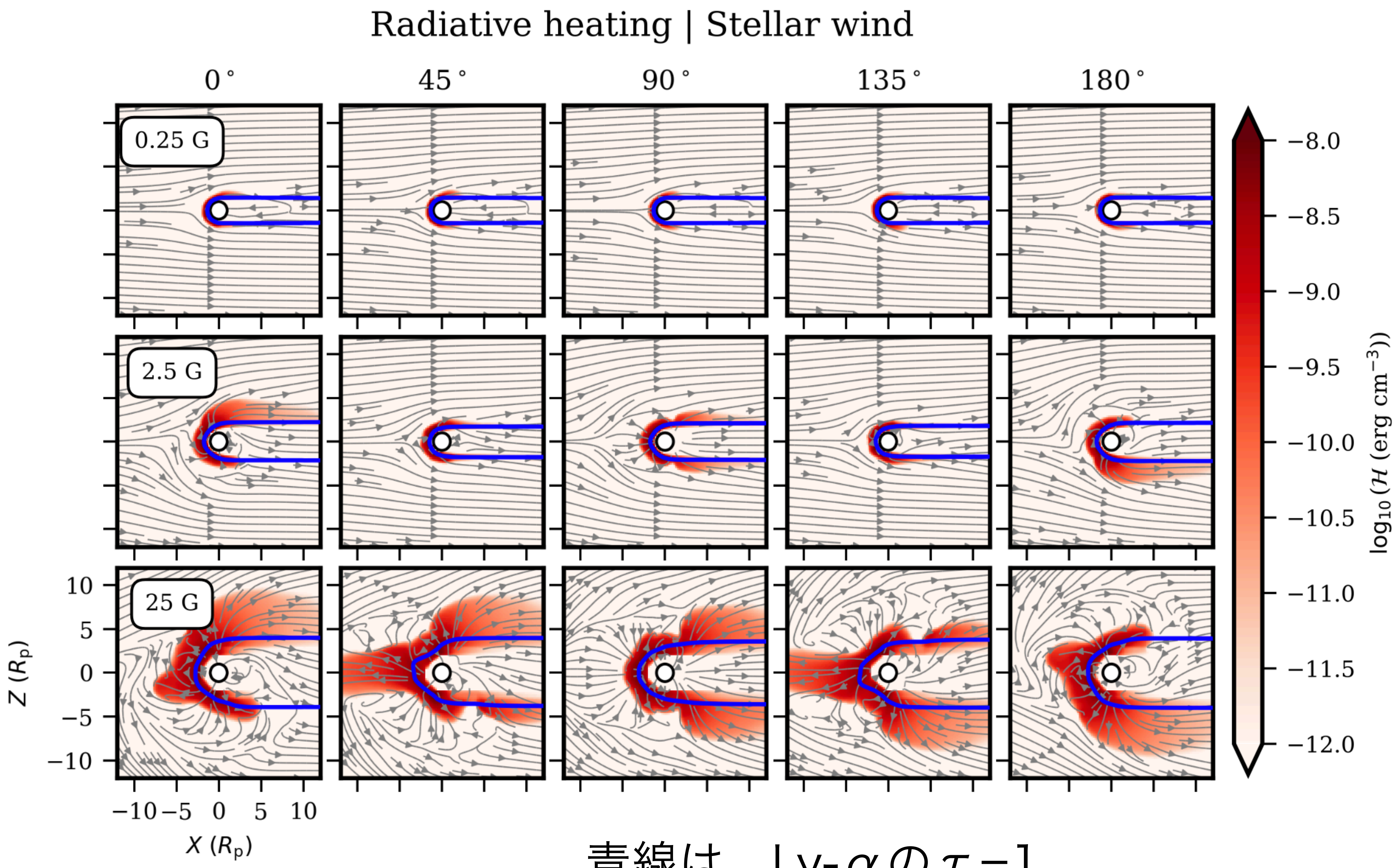

青線は，Ly-αのτ=1

Figure 2. Slice along the polar plane for selected models. Each row corresponds to a different magneti
a different magnetic obliquity. The colors indicate the density structure around the planet, and the gre
with no stellar wind. (Bottom) models with a stellar wind mass-loss rate of $2 \times 10^{-13}\ M_\odot$/yr.

Unmagnetised / weakly magnetised
Sub- or super-Alfvénic

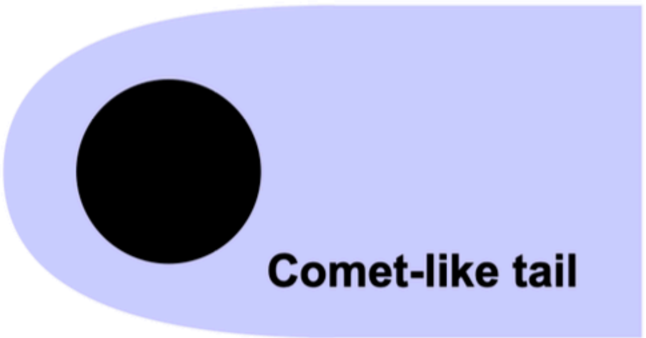

Sub-Alfvénic
(Radial stellar field)

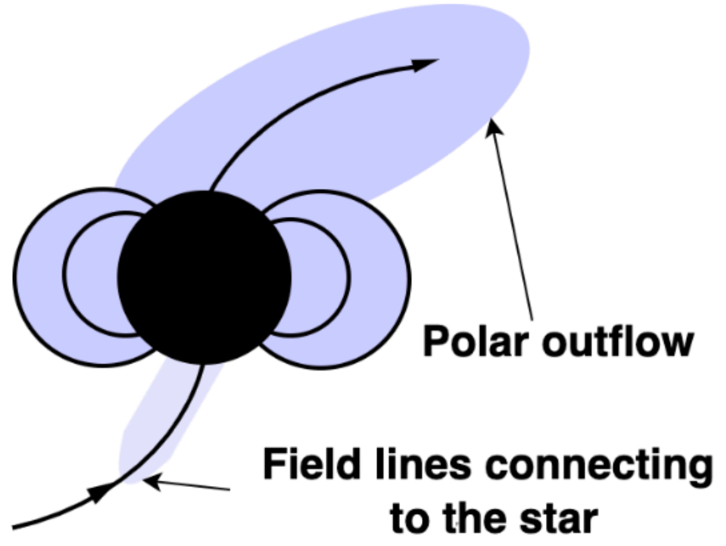

sents the radiative volumetric heating rate around the planet, while the grey streamlines trace the velocity
vhere the optical depth τ for the Lyman-α photons reaches unity.

磁場の強さと質量放出率

磁場が強いと，質量放出量が大きい（加熱率も大きい）

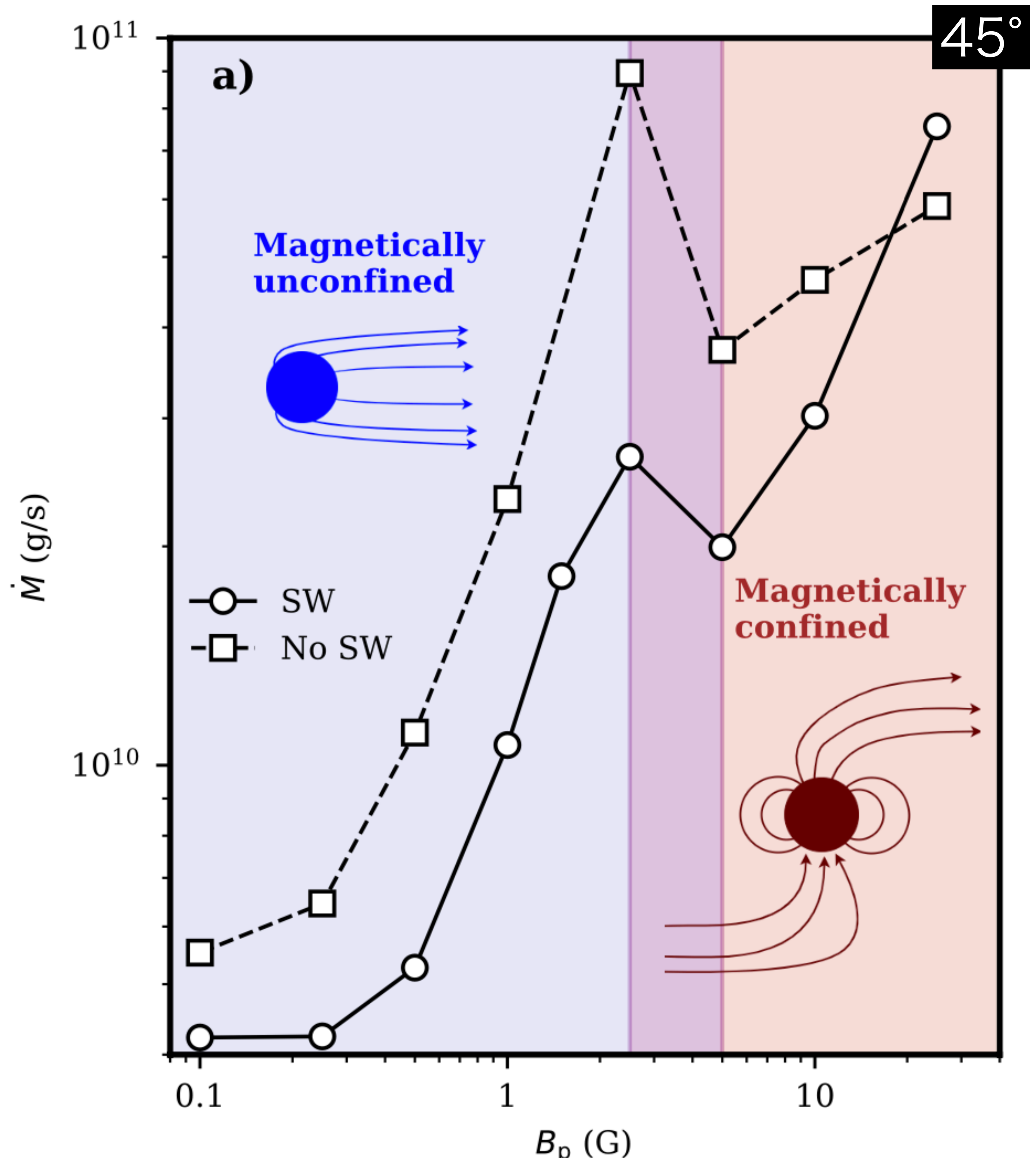

Figure 4. a) Atmospheric mass-loss rate as a function of the planetary magnetic field for a magnetic obliquity of 45°. The circles and solid lines represent the models with stellar wind, and the squares and dashed lines represent the models with no stellar wind.

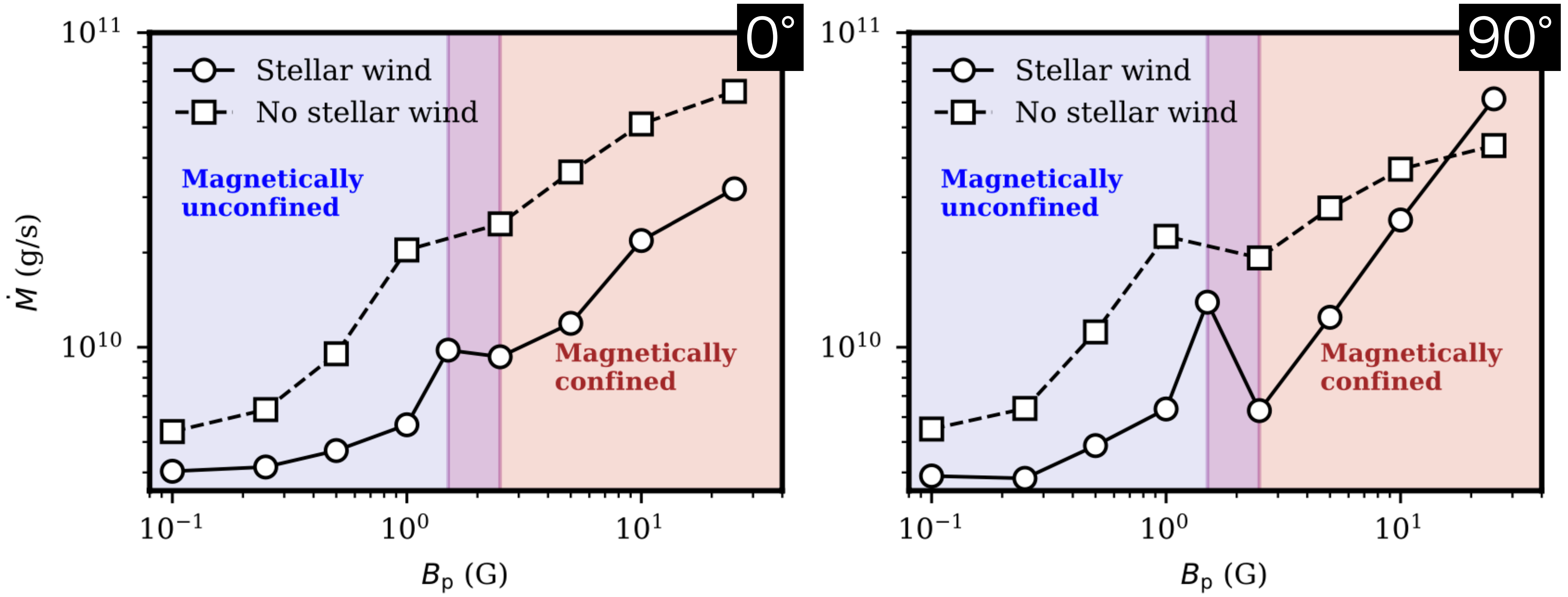

Figure A1. Similar to Figure 4a, for magnetic obliquities of 0° (left) and 90° (right).

X方向から観測したときのLy-αのtransit depthの計算

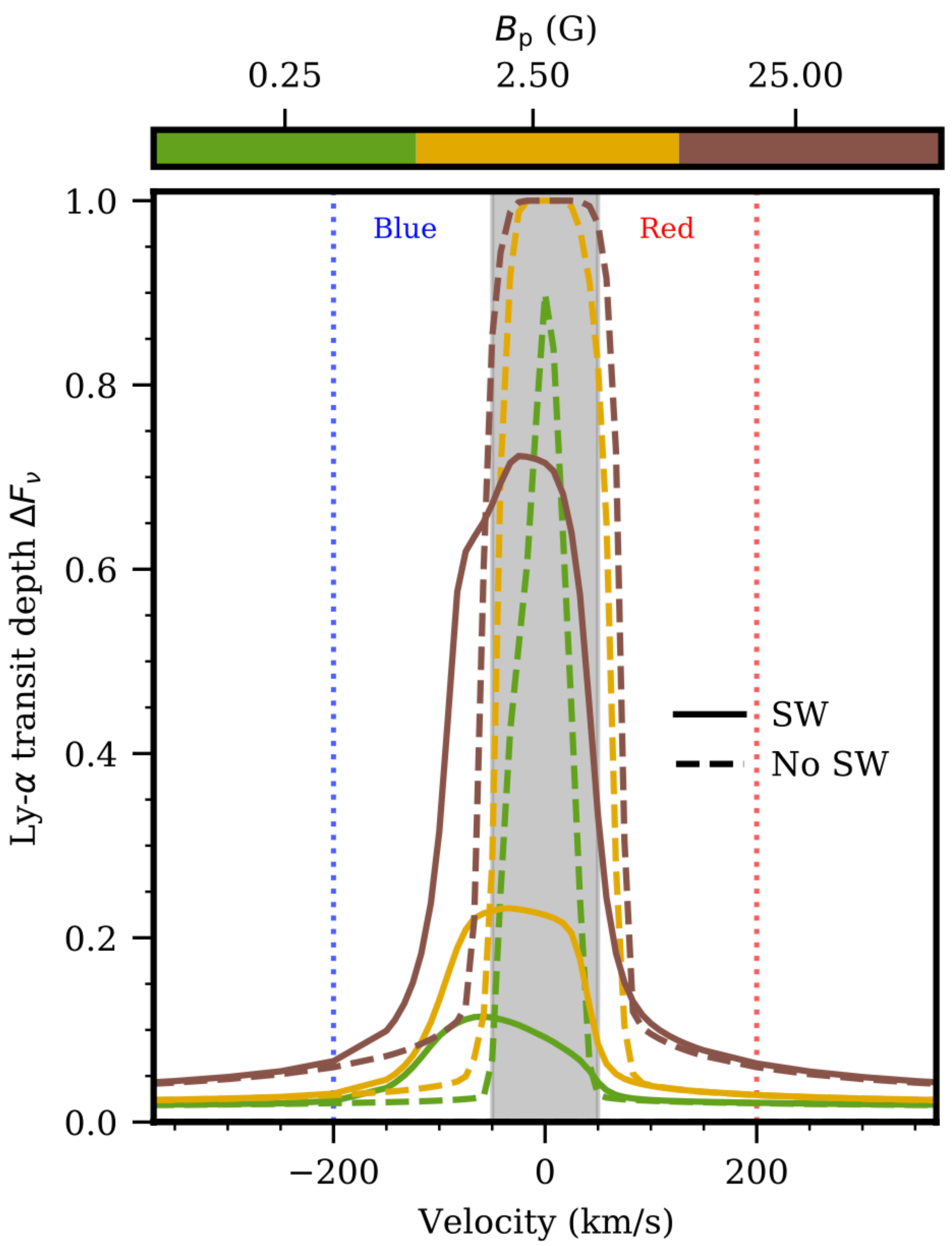

Figure 5. Transit depth of the Ly-α line at mid-transit for models with three magnetic field strengths with stellar wind (solid lines) and no stellar wind (dashed lines), assuming 0° magnetic obliquity. The blue and red vertical lines denote the outer bounds for the integrals of the blue and red wing absorptions considered in Figure 6, while the gray shaded area represents the line centre.

- 磁場が強くなると，中心吸収が大きい。
- 恒星風があるときは，磁場が強くなると，blue wingの吸収が大きい
  （観測者の方向に運動している惑星大気の影響）

議論：磁極の傾きによる違い

Bp＝5G

色は密度,
矢印は磁力線

色は中性ガスの密度,
矢印は流線

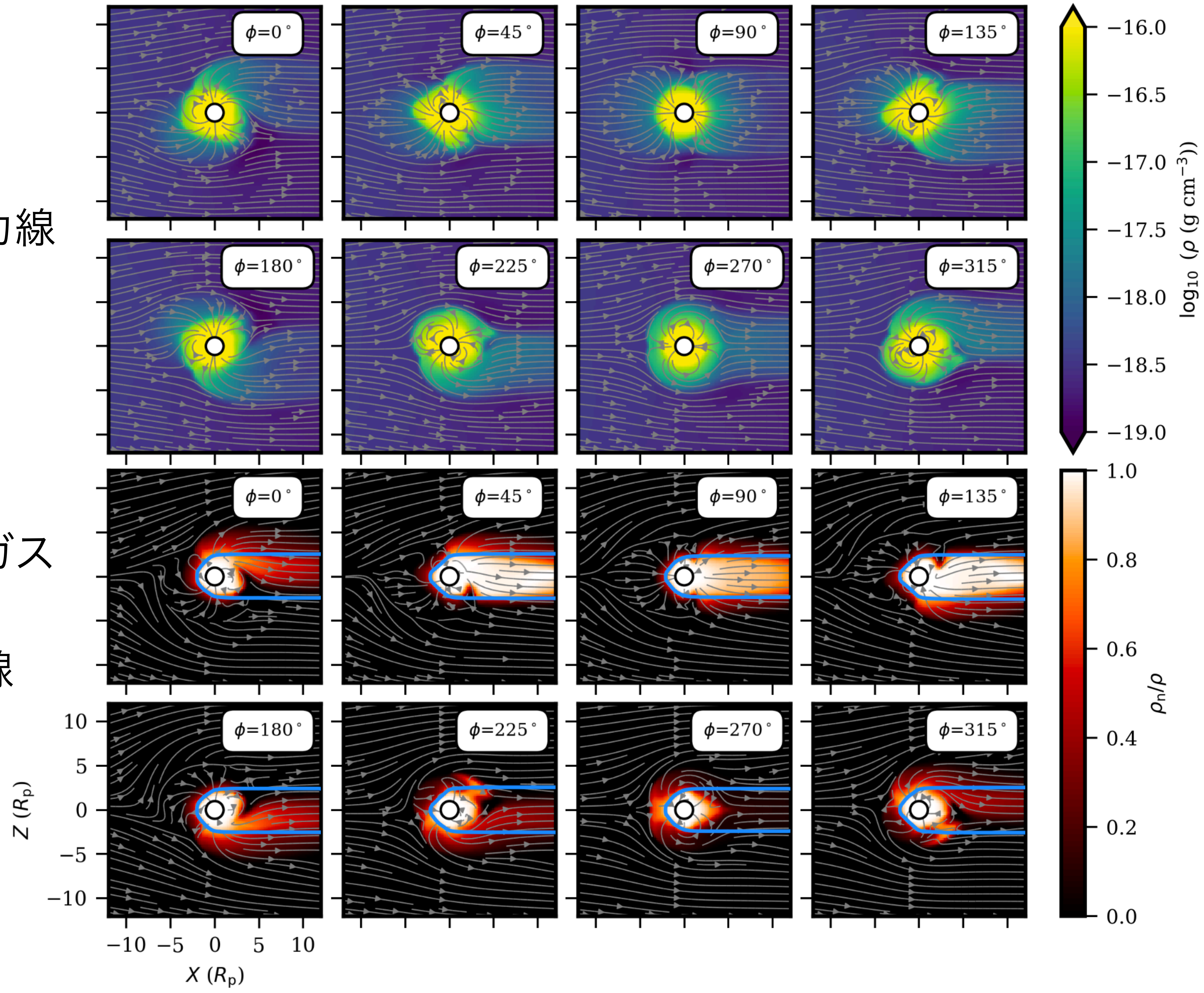

Figure 8. Polar plane cuts for different models with B_p = 5 G and different magnetic obliquities ranging from 0° degrees to 315°. The first two rows show the total density distribution, and the streamlines trace the magnetic field lines of each model. The last two rows show the density of neutrals normalized to the total density. In this case, the grey streamlines represent the velocity flow around the planet. The blue lines indicate the τ = 1 surface.

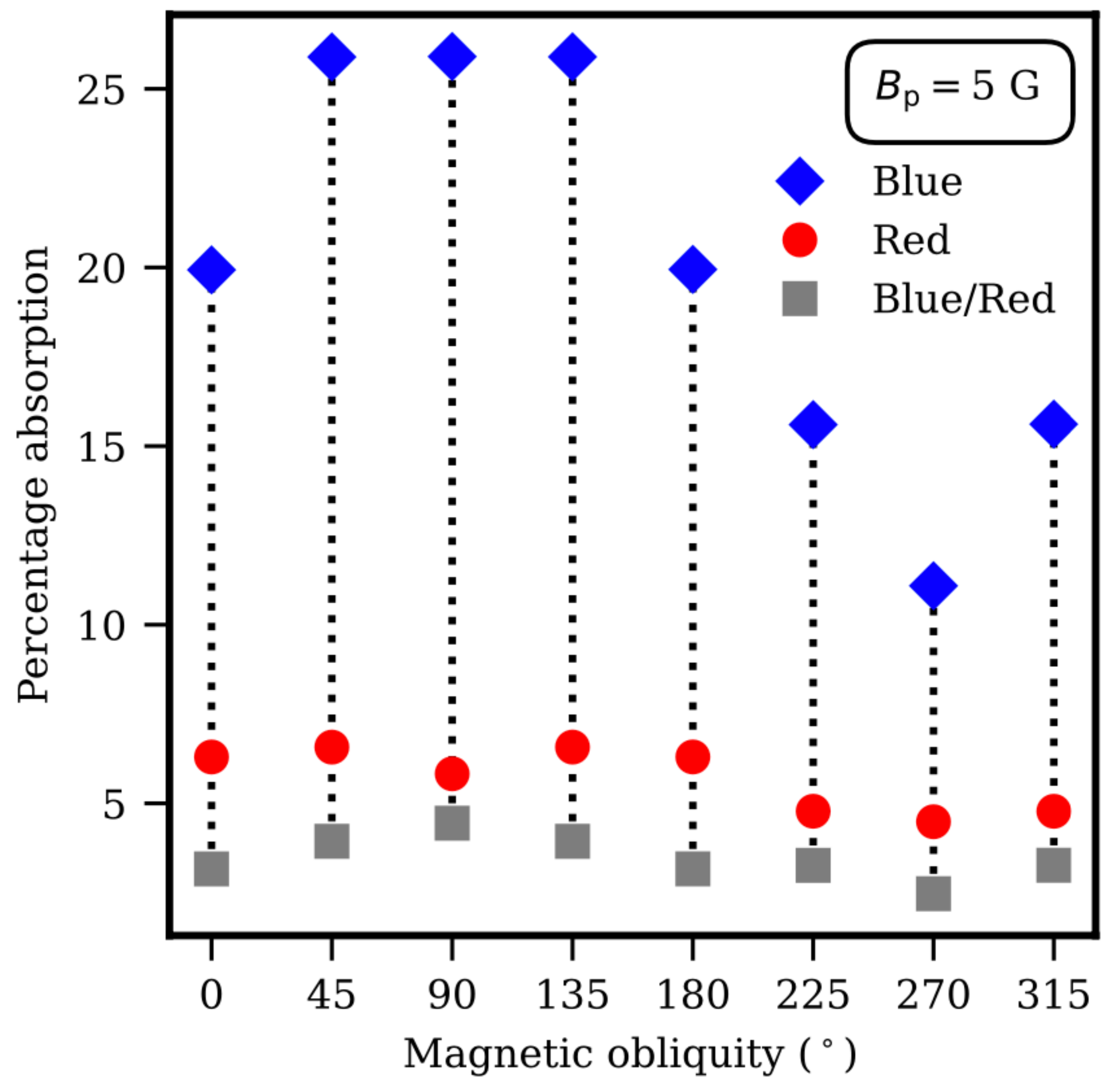

Figure 9. Ly-α absorption in the blue (blue diamonds) and red (red circles) wings, along with their blue-to-red ratios (grey squares) for B_p = 5 G and magnetic obliquity ranging from 0° to 315°. The integration bounds for the blue and red wing absorptions are the same as those used in Figure 6.

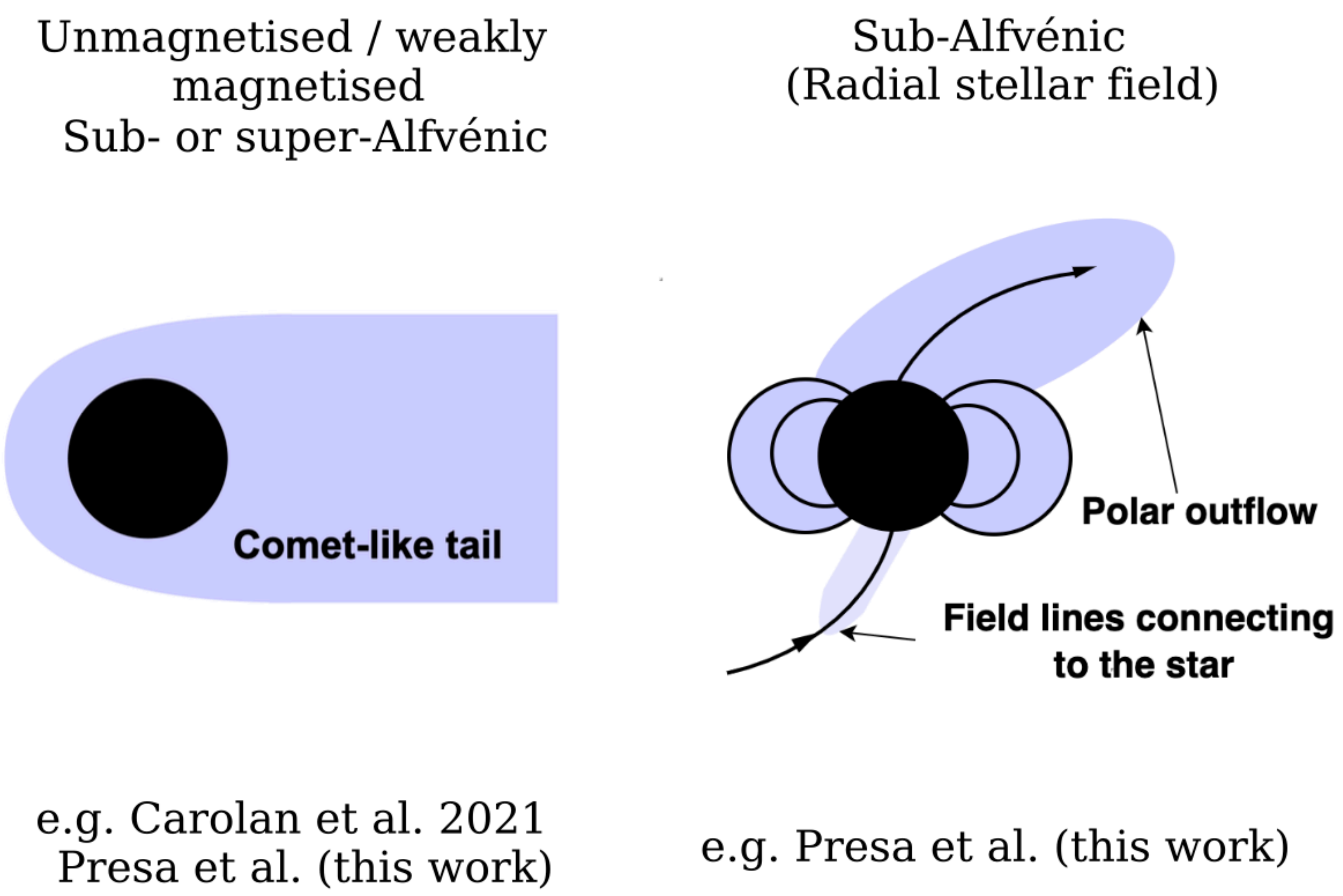

Astrophysics > Solar and Stellar Astrophysics

[Submitted on 11 Oct 2024]

BD+44 493: Chemo-Dynamical Analysis and Constraints on Companion Planetary Masses from WIYN/NEID Spectroscopy

Vinicius M. Placco, Arvind F. Gupta, Felipe Almeida-Fernandes, Sarah E. Logsdon, Jayadev Rajagopal, Erika M. Holmbeck, Ian U. Roederer, John Della Costa, Pipa Fernandez, Eli Golub, Jesus Higuera, Yatrik Patel, Susan Ridgway, Heidi Schweiker

In this work, we present high-resolution (R~100,000), high signal-to-noise (S/N~800) spectroscopic observations for the well-known, bright, extremely metal-poor, carbon-enhanced star BD+44 493. We determined chemical abundances and upper limits for 17 elements from WIYN/NEID data, complemented with 11 abundances re-determined from Subaru and Hubble data, using the new, more accurate, stellar atmospheric parameters calculated in this work. Our analysis suggests that BD+44 493 is a low-mass (0.83Msun) old (12.1-13.2Gyr) second-generation star likely formed from a gas cloud enriched by a single metal-free 20.5Msun Population III star in the early Universe. With a disk-like orbit, BD+44 493 does not appear to be associated with any major merger event in the early history of the Milky Way. From the precision radial-velocity NEID measurements (median absolute deviation - MAD=16m/s), we were able to constrain companion planetary masses around BD+44 493 and rule out the presence of planets as small as msin(i)=2MJ out to periods of 100 days. This study opens a new avenue of exploration for the intersection between stellar archaeology and exoplanet science using NEID.

- 超低金属星BD+44 493の高分解能，高SN比の観測を行い，元素組成を決定した。
- 質量（0.8Msun），年齢（12.1-13.1Gyr）を推定。元素組成の起源として，20.5MsunのPopIII単体の超新星爆発を推定。
- 星の銀河系での軌道を推定し，円盤内にいることが判明（ハロー星ではない）。
- 木星の2倍程度の質量を持つ惑星が，公転周期100日以内にはいないことがわかった。

恒星の物理量のまとめ

Table 1. Properties of BD+44 493

Quantity	Symbol	Value	Units	Reference
Right ascension	α (J2000)	02:26:49.74	hh:mm:ss.ss	Gaia Collaboration et al. (2022)
Declination	δ (J2000)	+44:57:46.5	dd:mm:ss.s	Gaia Collaboration et al. (2022)
Galactic longitude	ℓ	140.134	degrees	Gaia Collaboration et al. (2022)
Galactic latitude	b	−14.699	degrees	Gaia Collaboration et al. (2022)
Gaia DR3 ID		341511064663637376		Gaia Collaboration et al. (2022)
Parallax	ϖ	4.8661 ± 0.0226	mas	Gaia Collaboration et al. (2022)
Inverse parallax distance	$1/\varpi$	$206.8^{+1.0}_{-0.9}$	pc	This study[a]
Distance	d	$204.3^{+1.1}_{-1.0}$	pc	Bailer-Jones et al. (2021)
Proper motion (α)	PMRA	118.221 ± 0.021	mas yr^{-1}	Gaia Collaboration et al. (2022)
Proper motion (δ)	PMDec	−32.068 ± 0.020	mas yr^{-1}	Gaia Collaboration et al. (2022)
V magnitude	V	9.075 ± 0.005	mag	Henden & Munari (2014)
G magnitude	G	8.863 ± 0.003	mag	Gaia Collaboration et al. (2022)
BP magnitude	BP	9.209 ± 0.003	mag	Gaia Collaboration et al. (2022)
RP magnitude	RP	8.327 ± 0.004	mag	Gaia Collaboration et al. (2022)
Color excess	$E(B-V)$	0.0230 ± 0.0009	mag	Schlafly & Finkbeiner (2011)
Bolometric correction	BC_V	−0.50 ± 0.03	mag	Casagrande & VandenBerg (2014)
Signal-to-noise ratio @3800Å	S/N	93	pixel^{-1}	This study
@4560Å		432	pixel^{-1}	This study
@5180Å		574	pixel^{-1}	This study
@6580Å		797	pixel^{-1}	This study
Effective Temperature	T_{eff}	5351 ± 51	K	This study
		5430 ± 150	K	Ito et al. (2013)
Log of surface gravity	$\log g$	3.12 ± 0.07	(cgs)	This study
		3.40 ± 0.30	(cgs)	Ito et al. (2013)
Microturbulent velocity	ξ	1.45 ± 0.10	km s^{-1}	This study
		1.30 ± 0.30	km s^{-1}	Ito et al. (2013)
Metallicity	[Fe/H]	−3.96 ± 0.09	dex	This study
		−3.83 ± 0.19	dex	Ito et al. (2013)
Radial velocity	RV	−150.445 ± 0.016	km s^{-1}	This study
Isochronal-based age		$10.3^{+2.9}_{-3.5}$	Gyr	This study
Kinematical-based age		$13.1^{+0.5}_{-0.9}$	Gyr	This study
Constrained age range		[12.1, 13.2]	Gyr	This study
Mass	M	$0.83^{+0.09}_{-0.05}$	$M_\odot$	This study
Galactocentric coordinates	(X, Y, Z)	(+8.36, +0.13, −0.03)	kpc	This study
Galactic space velocity	(U, V, W)	(+33.5, −181.5, +51.5)	km s^{-1}	This study
Total space velocity	V_{Tot}	+191.6	km s^{-1}	This study
Apogalactic radius	R_{apo}	+8.623 ± 0.002	kpc	This study
Perigalactic radius	R_{peri}	+1.366 ± 0.011	kpc	This study
Max. distance from the Galactic plane	$z_{\max}$	1.286 ± 0.001	kpc	This study
Orbital eccentricity	ecc	0.726 ± 0.002		This study
Vertical angular momentum	L_Z	$(+0.728 \pm 0.004) \cdot 10^3$	kpc km s^{-1}	This study
Total orbital energy	E	$(-1.779 \pm 0.001) \cdot 10^5$	$\mathrm{km}^2\ \mathrm{s}^{-2}$	This study

[a]Using $\varpi_{\mathrm{zp}} = -0.0314$ mas from Lindegren et al. (2020).

恒星の吸収線

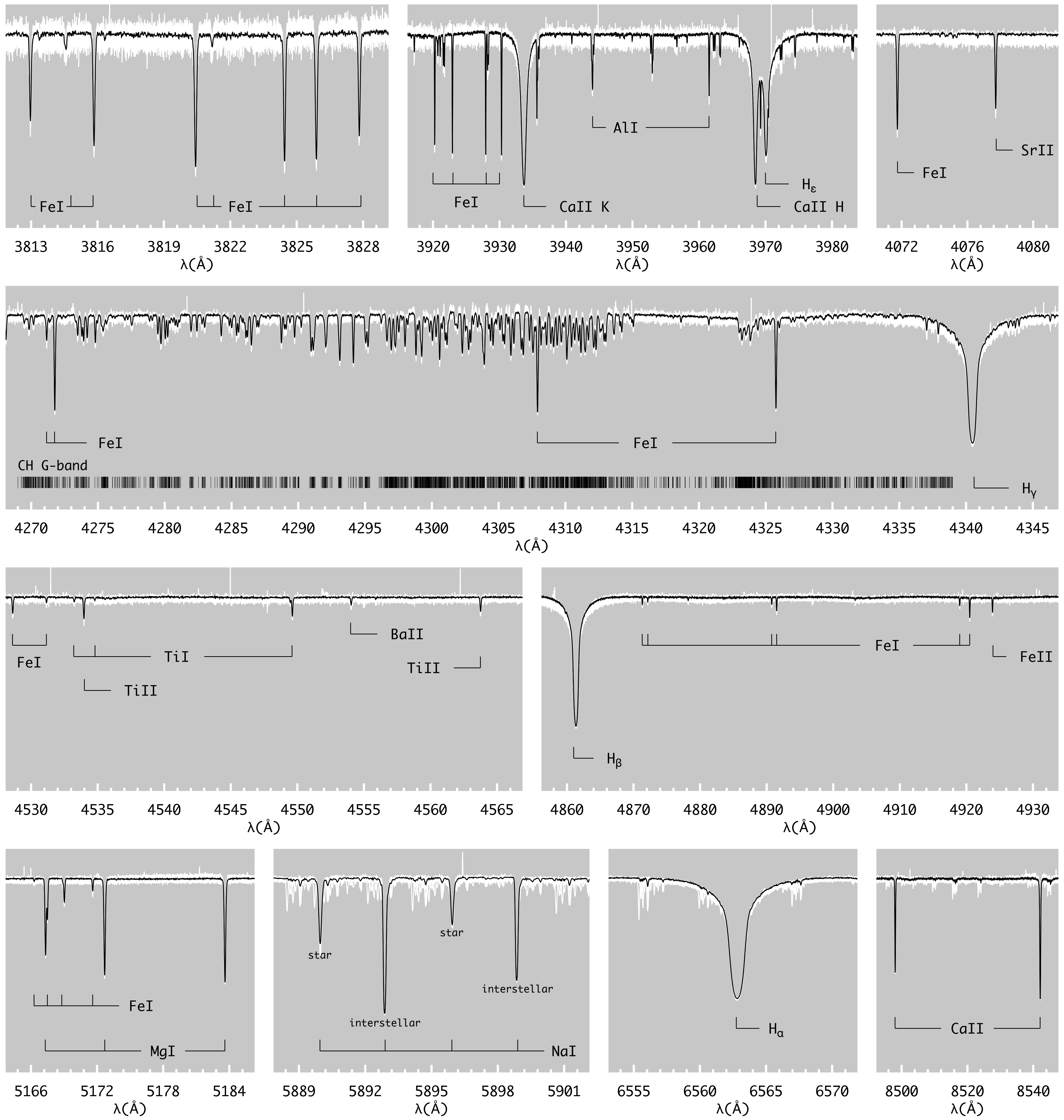

Figure 1. Normalized flux as a function of wavelength (in Å) for selected regions of the NEID spectra, highlighting a few absorption features of interest for stellar parameter and chemical abundance calculations. The solid black line represents the combined spectra and the white lines show the range of normalized fluxes for the individual exposures.

以前の観測　　今回の観測

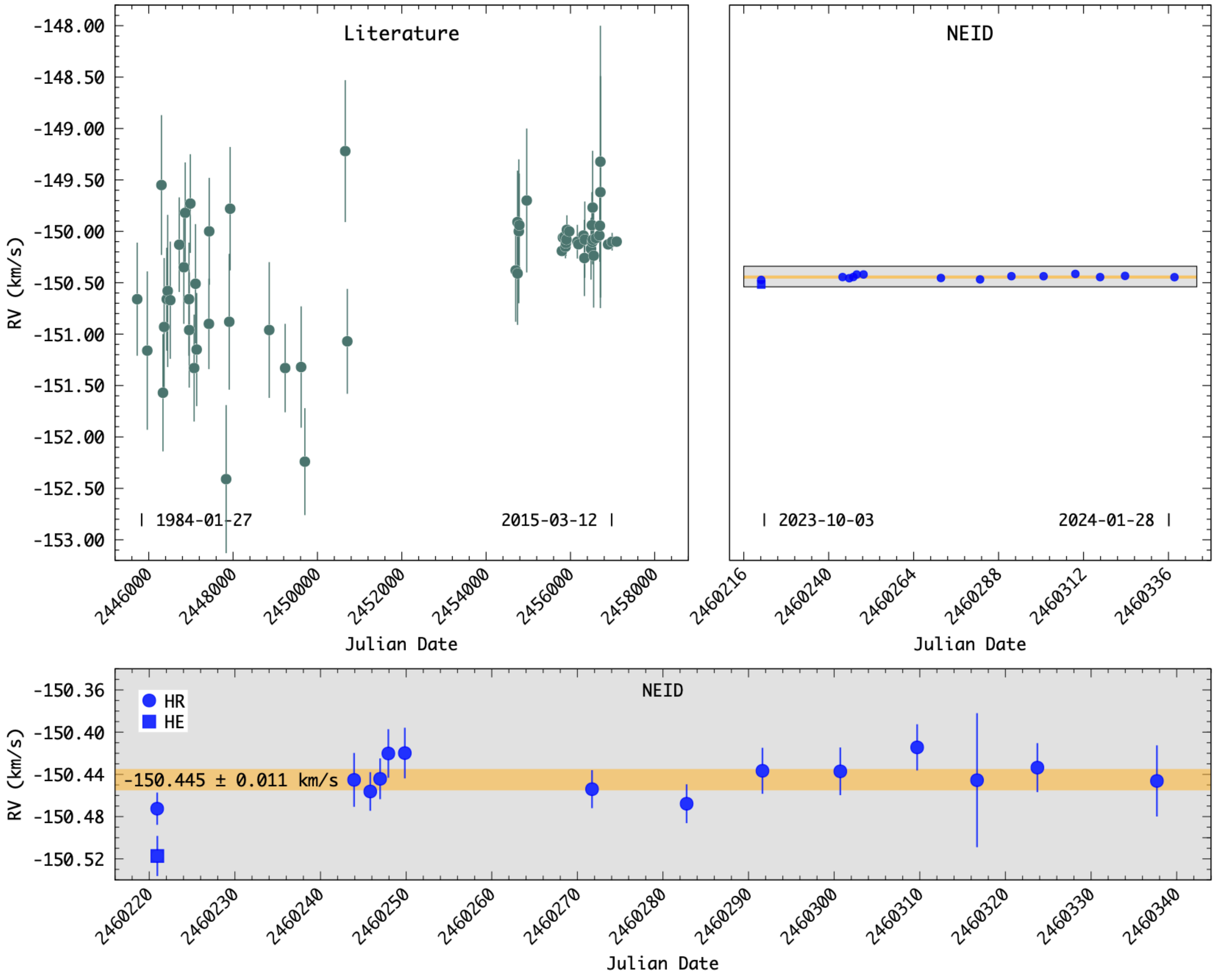

Figure 2. Top: Radial velocities for BD+44°493 from the literature (left) and from NEID (right). Individual measurements and references can be found in Tables 2 and 9. Bottom: Zoom in for the NEID radial velocities, with the median and median absolute deviation values annotated. The thickness of the horizontal line is proportional to 1σ.

視線方向速度の精度が高い

- 恒星の銀河軌道の決定
- 惑星の有無

今回の観測の拡大図

過去の研究（Ito et al.2013)との比較

重元素組成

Table 4. LTE Abundances for Individual Species

Species	log $\epsilon_{\odot}$ (X)	log ϵ (X)	[X/H]	[X/Fe]	σ	N	Ref.
Li I	1.05	0.86	−0.19	3.77	0.10	1	1
C [a]	8.43	5.87	−2.56	1.40	0.10	1	1
N	7.83	3.90	−3.93	0.03	0.20	1	2
O	8.69	6.25	−2.44	1.52	0.20	2	2/3
Na I	6.24	2.61	−3.63	0.33	0.03	2	1
Mg I	7.60	4.25	−3.35	0.61	0.12	8	1
Al I	6.45	1.94	−4.51	−0.55	0.10	1	1
Si I	7.51	3.90	−3.61	0.35	0.10	1	1
P I	5.41	1.04	−4.37	−0.41	0.21	3	4
S I	7.12	3.37	−3.75	0.21	0.41	3	4
Ca I	6.34	2.73	−3.61	0.35	0.11	7	1
Sc II	3.15	−0.61	−3.76	0.20	0.10	1	1
Ti I	4.95	1.39	−3.56	0.40	0.07	7	1
Ti II	4.95	1.19	−3.76	0.20	0.04	10	1
V II	3.93	−0.15	−4.08	−0.12	0.15	2	2
Cr I	5.64	1.28	−4.36	−0.40	0.03	2	1
Cr II	5.64	2.06	−3.58	0.38	0.21	2	4
Mn I	5.43	0.40	−5.03	−1.07	0.03	2	1
Mn II	5.43	0.75	−4.68	−0.72	0.02	3	2
Fe I	7.50	3.54	−3.96	0.00	0.09	123	1
Fe II	7.50	3.57	−3.93	0.03	0.09	6	1
Co I	4.99	1.47	−3.52	0.44	0.07	4	1
Co II	4.99	1.55	−3.44	0.52	0.23	4	4
Ni I	6.22	2.34	−3.88	0.08	0.05	2	1
Ni II	6.22	2.09	−4.13	−0.17	0.21	3	4
Cu I	4.19	−1.04	−5.23	−1.27	0.15	1	2
Zn II	4.56	0.33	−4.23	−0.27	0.24	1	4
Sr II	2.87	−1.41	−4.28	−0.32	0.10	2	1
Ba II	2.18	−2.53	−4.71	−0.75	0.10	2	1
Eu II	0.52	< −2.62	< −3.14	< 0.82	···	1	1

References—(1) WIYN/NEID (This work); (2) Subaru/HDS (Ito et al. 2013); (3) HST/STIS (Placco et al. 2014b); (4) HST/COS (Roederer et al. 2016).

[a] No evolutionary corrections from Placco et al. (2014a).

Table 5. NLTE Abundances for Individual Species

Species	log $\epsilon_{\odot}$ (X)	log ϵ (X)	[X/H]	[X/Fe]	σ	N
Li I	1.05	0.87	−0.18	3.59	0.10	1
Na I	6.24	2.60	−3.64	0.13	0.04	2
Mg I	7.60	4.41	−3.19	0.58	0.12	8
Al I	6.45	2.54	−3.91	−0.14	0.10	1
Si I	7.51	4.01	−3.50	0.27	0.10	1
Ca I	6.34	2.88	−3.46	0.31	0.14	6
Ti II	4.95	1.27	−3.68	0.09	0.04	10
Cr I	5.64	2.09	−3.55	0.22	0.05	2
Mn I	5.43	1.35	−4.08	−0.31	0.05	2
Fe I	7.50	3.73	−3.77	0.00	0.10	120
Fe II	7.50	3.57	−3.93	−0.16	0.10	6

基本的には同じ

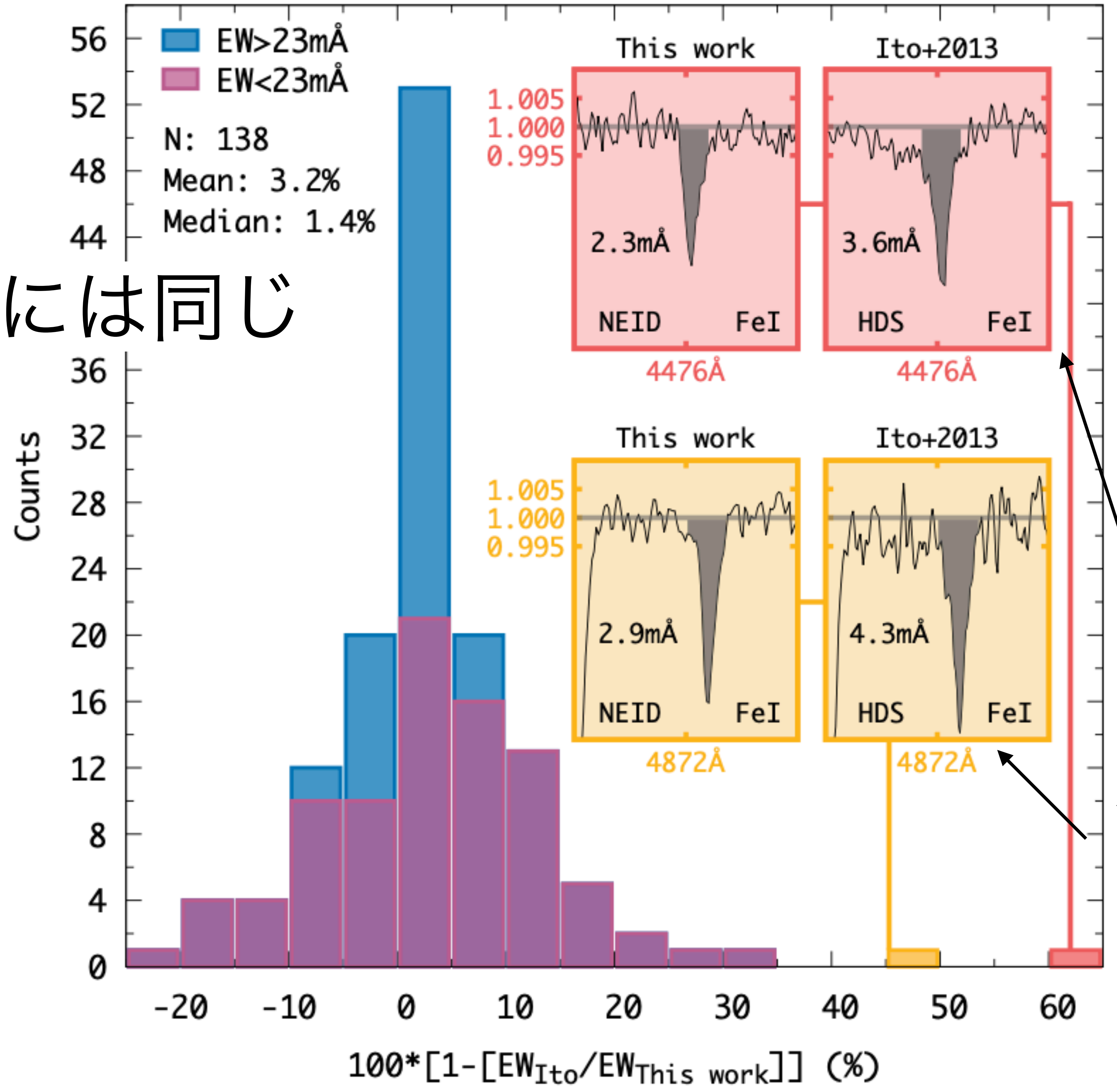

大きく異なった2つは弱い吸収線

Figure 6. Distribution of percent differences in equivalent width (in mÅ) for the 138 absorption features in common with the Ito et al. (2013) analysis. The mean and median differences are shown in the upper left. The red and yellow insets show the lines with the largest percent differences, highlighting the continuum placement in each case (NEID on the left, HDS on the right). See text for further details.

元素組成を再現する，PopIII星の超新星爆発モデルとの比較

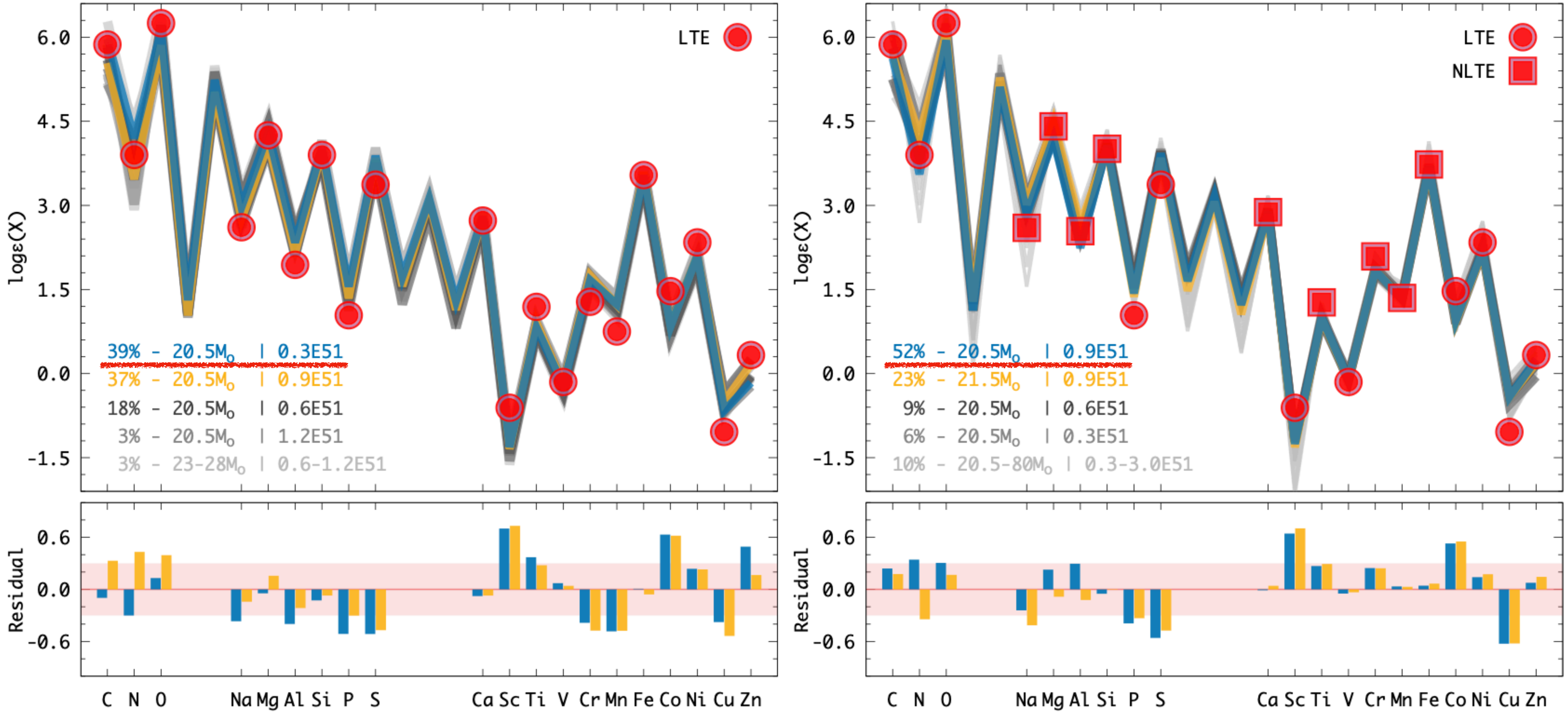

赤丸：観測
線：モデル

Figure 7. Upper panels: BD+44°493 light-element abundances (filled circles represent LTE values - left panels - and filled squares represent NLTE values - right panels) compared with yields from metal-free supernova models (solid lines). The labels show each model's progenitor masses, explosion energies, and their percentage occurrence among the 10,000 resamples of the BD+44°493 abundances. Lower panel: residuals between the observations and the two best-fit models. A ±0.3 dex shaded area is shown for reference.

20.5 Msun のメタルなしのPopIII星が超新星爆発を起こして周囲にばらまくガスの元素組成に近い

銀河系内の恒星の軌道計算

銀河系の重力場は変化しないことを仮定

ecc

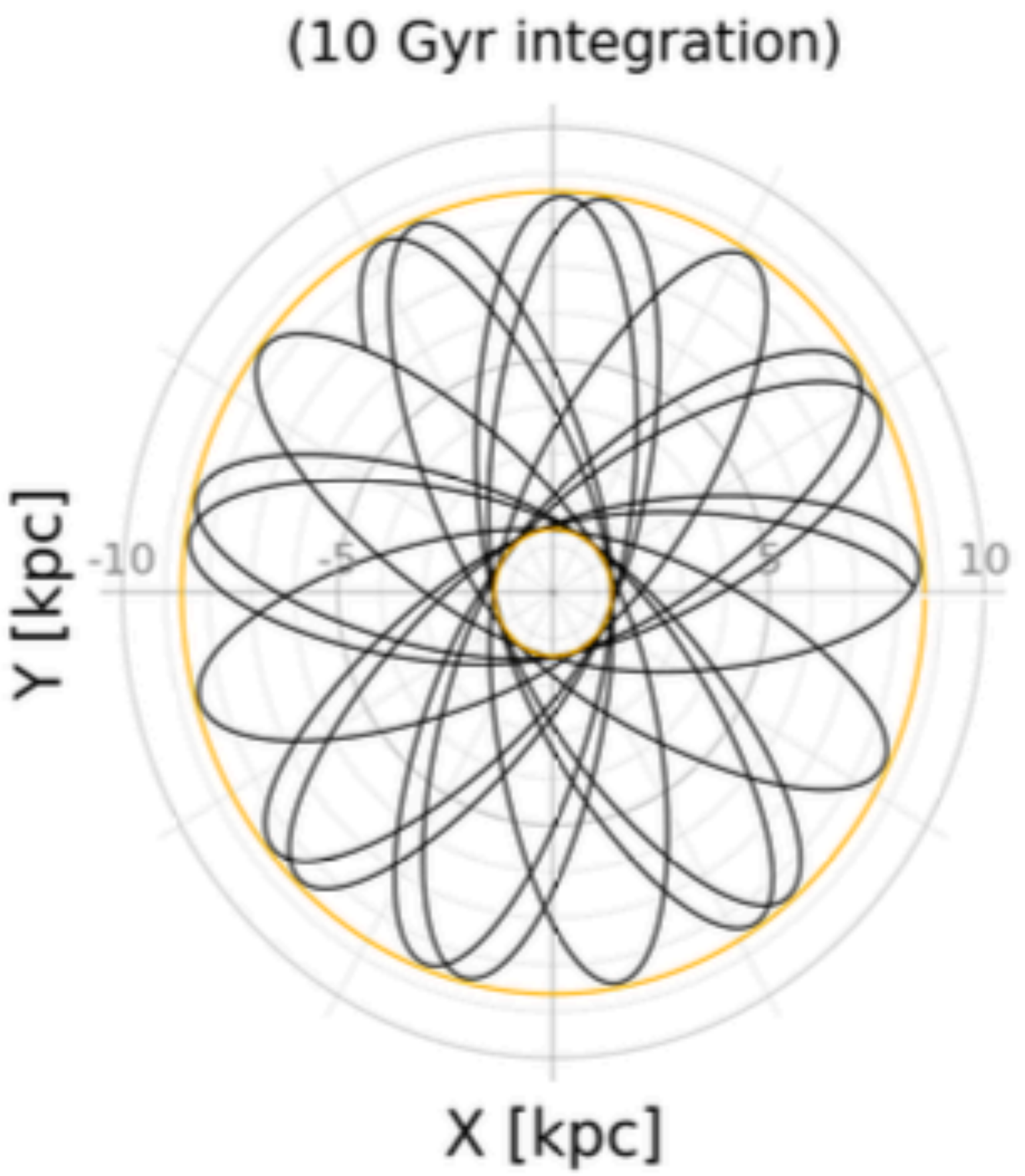

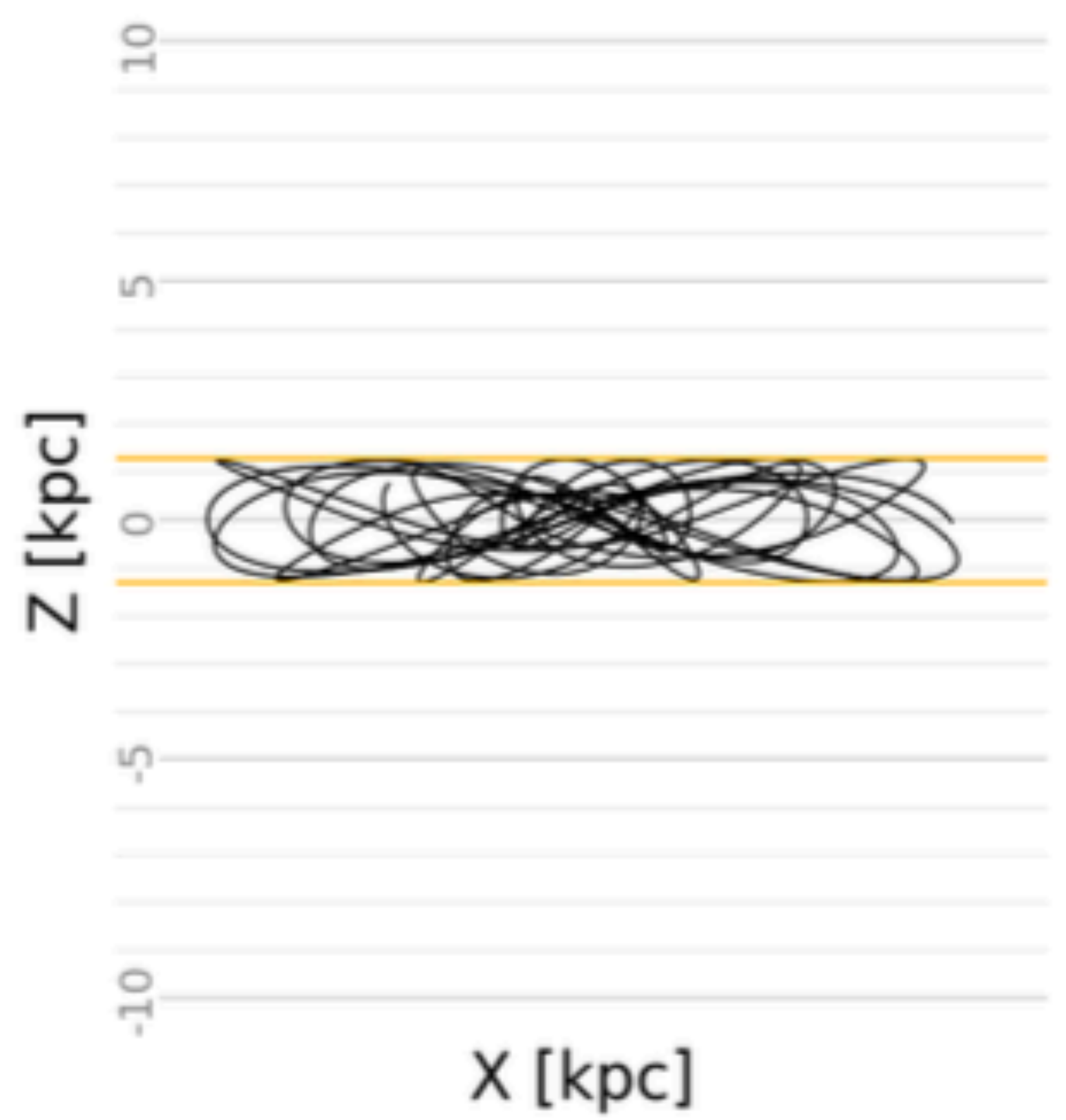

銀河円盤の中にある。

超低金属星で軌道が円盤内にあるもの

Table 7. Parameters of BD+44°493 and other UMP stars with similar orbital properties. All parameters were derived in this work, except for the metallicities of SDSS J0140, HE 1012−1540, LAM J1253, which were compiled by Sestito et al. (2019). Star names SDSS J0140 and LAM J1253 are abbreviated names for SDSS J014036.21+234458.1 and LAMOST J125346.09+075343.1, respectively.

Star	*ecc*	$z_{\max}$	$E/10^5$	$L_z/10^3$	[Fe/H]
		kpc	km^2 s^{-2}	kpc km^{-1}	dex
BD+44°493	0.73	1.28	−1.78	0.541	−3.96 ± 0.09
SDSS J0140	0.70	1.85	−1.64	0.796	−4.00 ± 0.30
HE 1012−1540	0.83	1.74	−1.58	0.558	−4.17 ± 0.16
LAM J1253	0.69	1.27	−1.61	0.885	−4.02 ± 0.06

年齢の推定

Isochroneから推定

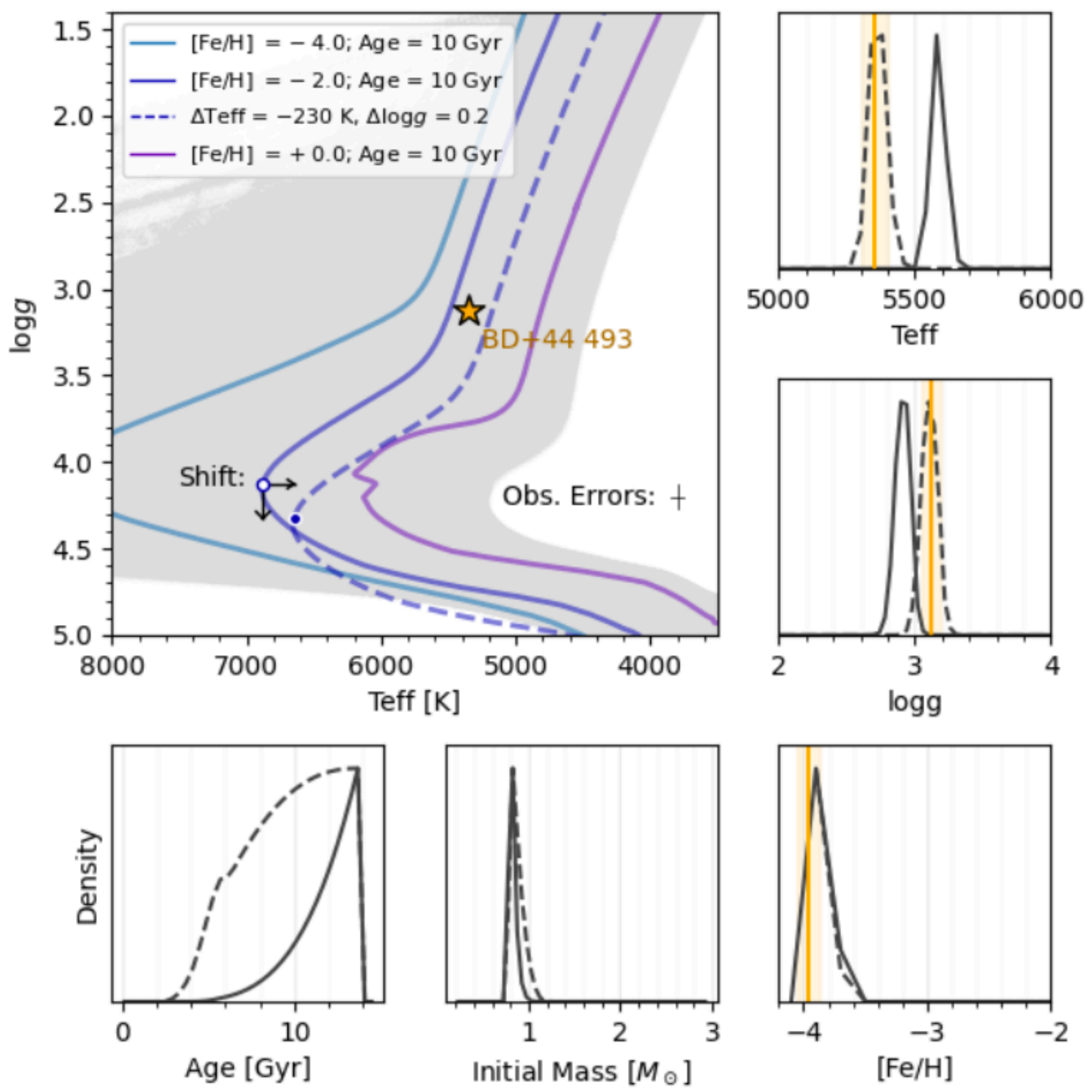

Figure 9. Top left: Kiel diagram for BD+44°493 (yellow star-shaped symbol) and the MIST model grid used in this work (grey area). For guidance, we highlight three isochrones of 10 Gyr and three different metallicities (−4.0, violet; −2.0, blue; 0.0, cyan). We also show the offset applied to the models (for simplicity, this is shown only for the −2.0 metallicity isochrone, represented by a dashed blue line). The observational errors for BD+44°493 are shown in the bottom-right corner. The right-side panels display the PDFs obtained by our method for effective temperature, surface gravity, and metallicity for the original models (solid lines) and the offset models (dashed lines), along with the true observational values (vertical yellow lines). The bottom-left and bottom-center panels display the obtained age and initial mass PDFs, for the original and offset models (solid and dashed lines, respectively).

5.4. *Kinematical Age*

We have also estimated a kinematical-based age for BD+44°493 from its heliocentric Galactic U, V, W velocities. The dispersion of these velocities for a group of stars has long been known to correlate with stellar ages (Wielen 1977). Based on this characteristic,

運動学的に推定

星が銀河内で歳をとるに連れて、軌道が重力的な相互作用などにより乱され、速度分散が増加する。

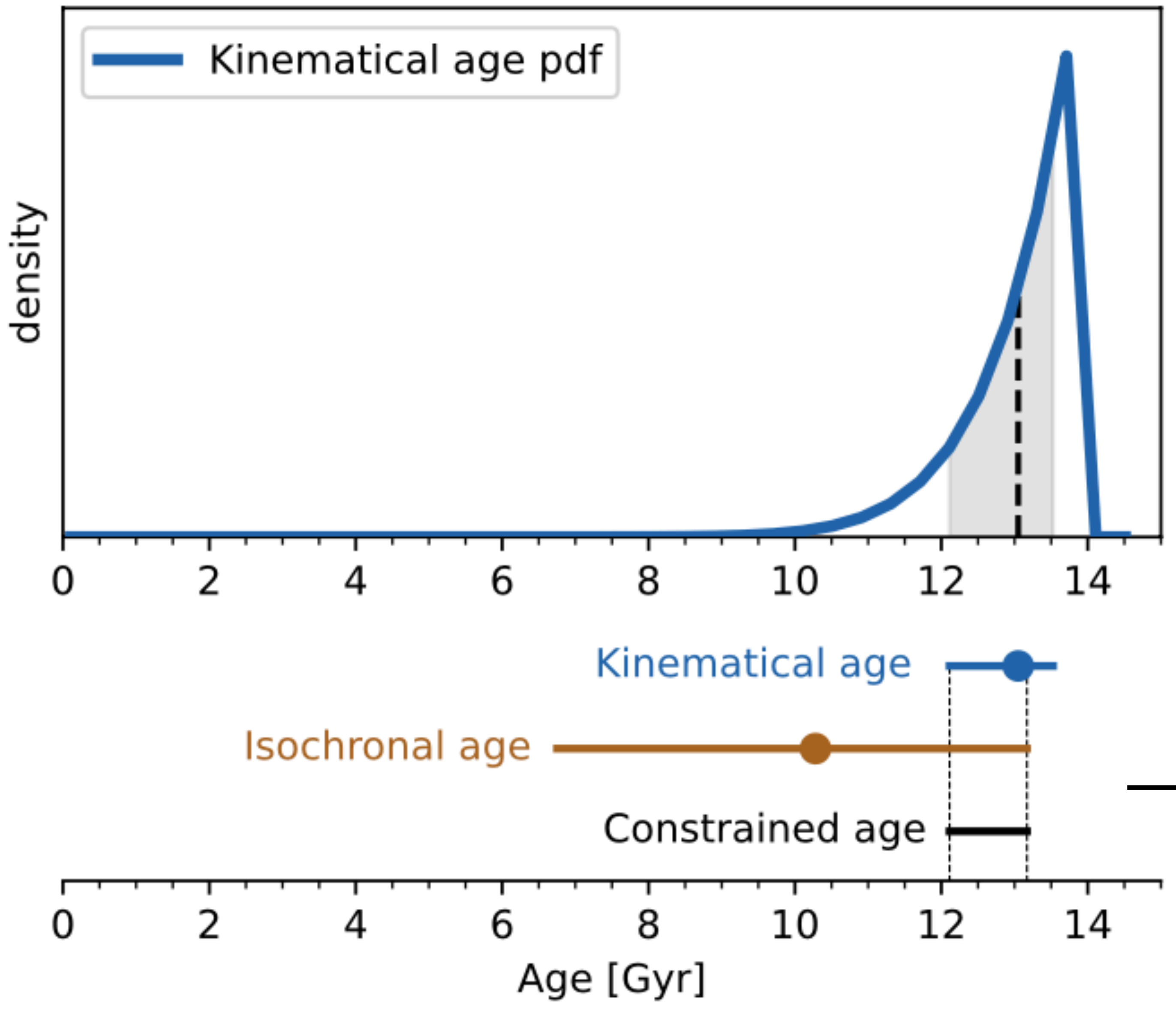

年齢（Gyr)

→ ～13Gyr

Figure 10. Top: Age PDF obtained for BD+44°493 from the heliocentric UVW Galactic velocities using the method from Almeida-Fernandes & Rocha-Pinto (2018a). Bottom: The median age obtained by the kinematical and isochronal methods is represented by blue and golden circles, respectively. The blue and golden lines represent the 16th and 84th age percentiles obtained for each method. The constrained age interval (shown as a black line) corresponds to the intersection of the age intervals from the previous methods.

パワースペクトル

視線方向速度の時間変化

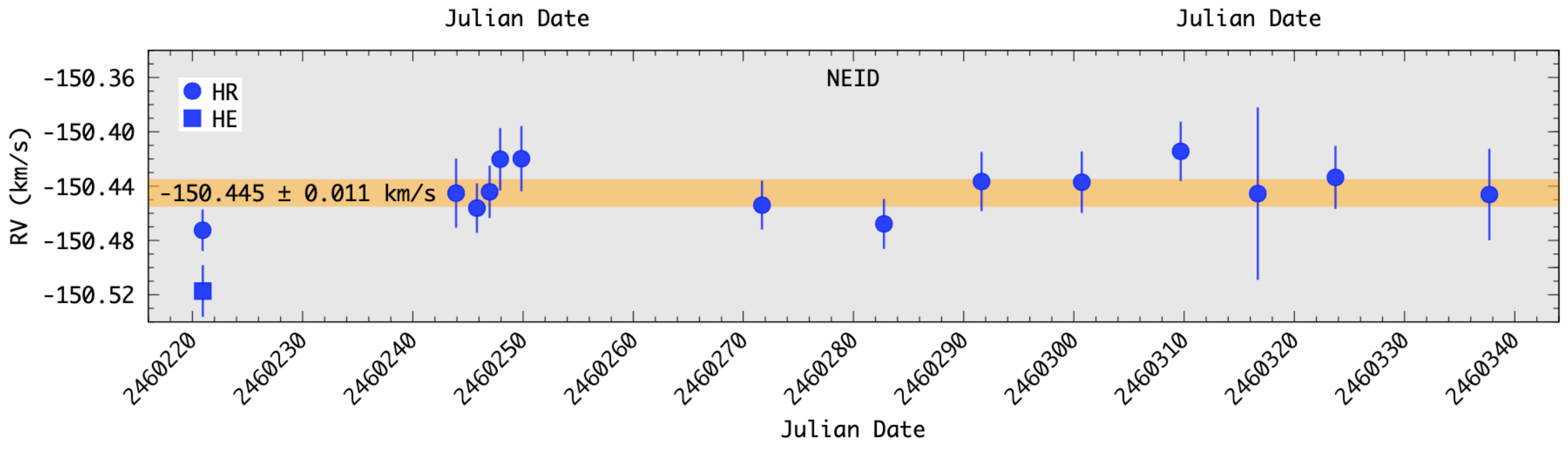

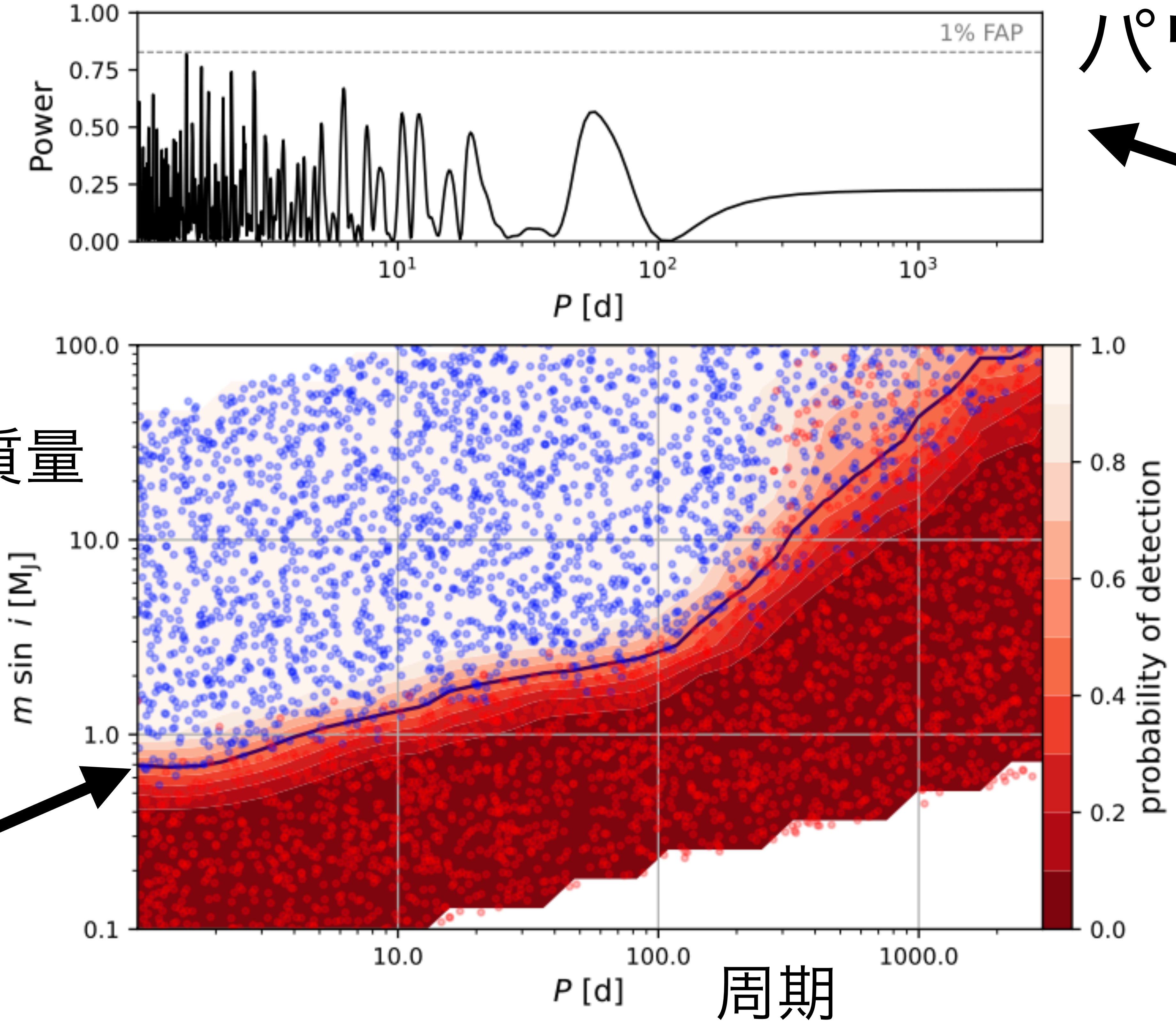

質量

50%

周期

惑星があったときに観測される
であろう確率

Figure 11. Upper panel: Generalized Lomb-Scargle periodogram of the NEID RV measurements of BD+44°493. No signals are detected above the 1% false alarm level threshold. Lower panel: Results of injection-recovery tests for NEID RV measurements of BD+44°493. Blue points are injected planets that are successfully recovered, and red points are those that would not be detected. The background shading indicates the recovery fraction across the mass-period grid that was tested, where white corresponds to a 100% recovery rate and deep red is a 0% recovery rate. We also show the 50% recovery threshold as a black line.